Journal of Materials Processing Technology 212 (2012) 1598–1610

Contents lists available at SciVerse ScienceDirect

Journal of Materials Processing Technology

journal homepage: www.elsevier.com/locate/jmatprotec

# Parametric study on a coaxial multi-material powder flow in laser-based powder deposition process

Prabu Balu, Perry Leggett, Radovan Kovacevic*

*RCAM (Research Center for Advanced Manufacturing), Southern Methodist University, 3101 Dyer St., Dallas, TX 75205, United States*

ARTICLE INFO

*Article history:*
Received 2 November 2011
Received in revised form 15 February 2012
Accepted 29 February 2012
Available online 8 March 2012

*Keywords:*
Laser-based powder deposition
Composite powder
Radially symmetric nozzles
Powder flow characteristics
Experimental technique
CFD simulation

ABSTRACT

The manner with which the composite powder particles injected into the laser formed molten pool decides the deposition quality in a typical laser-based powder deposition of composite material. Since, the morphology and physical properties of nickel (Ni) and tungsten carbide (WC) are different their powder flow characteristics such as the powder particles stream structure, maximum concentration at the converging spot, and the powder particles velocity are noticeably different. In the current study, a computational fluid dynamics (CFD) based powder flow model is established to characterize the coaxial powder flow behavior of Ni–WC composite powders. The key powder flow characteristics such as the stand-off distance, the diameter of the powder stream at the stand-off distance, and the velocity of the powder particles are measured using three different vision based techniques. Both the numerical and experimental results reveal the exact stand-off distance where the substrate needs to be placed, the diameter of the concentration spot of powder at the stand-off distance, and a combination of suitable nozzle angle, diameter, and carrier gas flow rate to obtain a maximum powder concentration at the stand-off distance with a stable composite powder flow.

© 2012 Elsevier B.V. All rights reserved.

## 1. Introduction

In a metal–ceramic laser-based powder deposition (LBPD), the composite powder particles are transported by an inert gas through a nozzle into the laser formed molten pool on a substrate, and the deposit as a mixture of ceramic dispersed in metal matrix is achieved by moving either the laser head or substrate with respect to each other. In a typical LBPD, the coaxial method of powder injection has gained a wide acceptance because of its capability for high productivity and for direction independent deposition with high precision (Weisheit et al., 2001).

One of the pivotal factors dictating the powder utilization efficiency, repeatability of depositing metal–ceramic composite material, track geometry and final metallurgical properties in the LBPD process is the powder flow characteristics. The key powder flow characteristics include the powder particles stream structure and concentration, the distance from the nozzle tip at which the maximum powder concentration occurs (stand-off distance), powder spot diameter at the converging spot, and the powder particles velocity. The precision control of these characteristics is influenced by numerous variables like the powder feeding nozzle diameter and its angle, career gas flow rate, powder particle size, morphology and its properties, etc. Understanding through experimentation the effect of individual variables that decides the powder flow characteristics in a typical LBPD process is difficult and time consuming. Choosing the appropriate design features of a powder feeding system and powder feeding conditions to achieve the desired characteristics is of interest. More importantly, the repeatability of achieving the desired deposit composition from the elemental powders of different material groups is challenging.

Several experimental, analytical and numerical modeling efforts have been reported to date to understand the powder flow characteristics and interactions of the powder particles/laser during the LBPD process. Picasso et al. (1994) estimated the laser energy attenuation by the powder stream via a lateral nozzle in a LBPD process. The powder stream is considered to be cylindrical in shape with constant radius. It is reported that the laser energy attenuation increases with an increase in the powder flow rate. Fu et al. (2002) proposed a theoretical model to estimate the temperature raise of the powder particles by the laser beam in a LBPD process. It is shown that the powder feeding angle significantly affects the powder particles temperature and the attenuation of laser energy. Pinkerton and Li (2004) proposed an analytical model to understand the powder stream behavior from a coaxial nozzle and the attenuation of laser energy by the powder stream. It is reported (Pinkerton and Li, 2004) that the maximum powder concentration occurs at the location where the powder stream from the nozzle merge together and the attenuation of laser energy increased with distance from

* Corresponding author.
*E-mail address:* kovacevi@lyle.smu.edu (R. Kovacevic).

0924-0136/$ – see front matter © 2012 Elsevier B.V. All rights reserved.
doi:10.1016/j.jmatprotec.2012.02.020

the nozzle exit. Similarly, Huang et al. (2005, 2006) developed a three-dimensional (3-D) analytical model to estimate the attenuation of laser energy by the heating of the powder particles, and the powder particles temperature distribution closer to the substrate surface in a LBPD process. The study revealed that an increase in both the nozzle angle with respect to horizontal plane and powder flow rate cause significant increase in the laser energy absorption by the powder particles subsequently lead to a drop in the laser peak intensity. Yang (2009) proposed a model to predict the maximum powder stream concentration in coaxial laser cladding for different powder properties, nozzle geometries and shielding gas settings. It is shown that the particle velocity and mass flow rate decide the powder stream structure and concentration distribution. Further, it is reported that the smaller nozzle diameter and smaller nozzle angle lead to a more focused powder stream with maximum concentration. Zhang et al. (2009) developed an analytical model and experimental procedure to control the composition of the mixed elemental powders of titanium, aluminum, and molybdenum during the coaxial powder flow in the LBPD process by assuming that the particles are of uniform spherical shape. It is demonstrated that the maintenance of a smaller and consistent divergence angle of different elemental powder streams at the nozzle exit can result in a chemical composition of deposited layer that is the same as that of the supplied premixed powders. Even though an analytical model is easy to apply, it lacks in providing more detailed effect of both the geometrical variation of the nozzle, and shape and morphology of the powder particles on powder flow characteristics.

A few numerical models are reported to understand the powder flow characteristics in a LBPD process. Lin (2000) showed that the powder stream from a coaxial nozzle follows a Gaussian concentration distribution and that the parameters of the distribution, stream angle, and powder catchment efficiency could be changed by controlling the shielding and carrier gas flows (Lin and Steen, 1998; Pan et al., 2006). Zekovic et al. (2007) performed a comprehensive study on the coaxial powder flow characteristics of the radially symmetric nozzles. The developed model is used to estimate the feasible stand-off distance to achieve a stable deposition and an appropriate convective boundary condition for the heat transfer calculations based on the gas flow velocity. Wen et al. (2009) presented a complete model to predict the powder flow characteristics incorporating the particle heating by laser. The outcome of their model includes a feasible stand-off distance to achieve maximum powder concentration, powder flow velocity, and particle temperature distribution as powder flow reaches the molten pool. Tabernero et al. (2010) modeled the powder flux distribution on a coaxial nozzle. The model is validated based on the measured powder flux distribution for AISI-316L stainless steel, AISI-D2 tool steel and INCONEL 718© Nickel based super alloy powders. Further, the calculated powder flux from the numerical model is supplied to the simple geometrical model to estimate the clad height. Recently, Kovalev et al. (2010) performed a detailed numerical and experimental study to estimate the powder flow characteristics and the particles heating due to laser irradiation in coaxial laser direct metal deposition process. The developed numerical model is used to study the effects of powder particles bouncing (elastic and non-elastic) at the nozzle interior wall, and the powder particles shape and size distribution on the powder flow characteristics. It is reported that the powder particles may exposed to melting and boiling temperature under the laser irradiation conditions.

However, no attempt has been reported in connection to the effect of the powders of different types of material groups on the powder flow characteristics such as stand-off distance, maximum powder concentration, and velocity of powder particles at the exit of the nozzle using both numerical and experimental approach. In addition, an influence of powder flow setup design variables such as nozzle diameter and nozzle angle on the powder flow characteristics is not well reported. Notably, a numerical model for predicting dispersed elemental powder flow of different types of material groups within the coaxial nozzle, including collision of powder with rough walls and irregular bouncing of non-spherical particles, is non-existent. This study deals with the development of an integrated numerical and experimental approach to understand the flow characteristics of the elemental powders that consists of both nickel (Ni) and tungsten carbide (WC).

Fig. 1 presents the 3D model of the powder feeding head with the nozzle holder used in this study. The powder, transported by the inert gas through four radially symmetrical nozzles at 60° to the horizontal axis, is delivered into the molten pool created by the laser beam. The powder feeder system features a variable speed control motor that allows adjustment of the powder mass flow rate as low as 0.2 g/min to a maximum of 50 g/min based on the rotational speed of the powder feeder rotating discs (Valant and Kovacevic, 2006). An adjustment slot (A) is provided to obtain a defocused spot diameter of the laser at the substrate. In a typical LBPD process this procedure is followed to achieve a wider deposition.

## 2. Numerical modeling formulation (Fluent 6.3, 2006)

In a typical LBPD process, the powder particles usually are carried by an inert gas. Thus, the problem is solved using the dispersed phase model available in the commercial computational fluid dynamics (CFD) code FLUENT in which, the gas phase and solid powder particle are treated as the continuous phase and discrete phase, respectively (Fluent 6.3, 2006).

### 2.1. Modeling of gas phase

The conservation of mass and momentum for the gas phase can be expressed as Eqs. (1) and (2)

$$\frac{\partial u_i}{\partial x_i} = 0 \tag{1}$$

where $u_i$ and $x_i$ represent the velocity and position in i direction.

$$\frac{\partial(\rho u_i u_j)}{\partial x_i} = -\frac{\partial p}{\partial x_i} + \frac{\partial \tau_{ij}}{\partial x_j} + \phi_i \tag{2}$$

where $p$, $g$, $\tau_{ij}$ and $\phi_i$ is the pressure, acceleration due to gravity, viscous stress tensor, and source term, respectively. The density of argon gas$\rho$ is 1.6228 kg/m$^3$. The $\tau_{ij}$ is given by

$$\tau_{ij} = \left[(\mu + \mu_t)\left(\frac{\partial u_i}{\partial x_j} + \frac{\partial u_j}{\partial x_i}\right)\right] - \frac{2}{3}\mu_t \frac{\partial u_i}{\partial x_i}\delta_{ij} \tag{3}$$

where μ is the molecular viscosity ($2.125 \times 10^{-5}$ kg/m-s), $\delta_{ij}$ the Kronecker delta that equals 1 when $i=j$, otherwise $\delta_{ij}=0$ and $\mu_t$, the turbulent viscosity is expressed as

$$\mu_t = \rho C_\mu \frac{k^2}{\varepsilon} \tag{4}$$

The source term, $\phi_i$ represents the coupled momentum transport from the particle phase that is expressed as

$$\phi_i = \frac{1}{V_c}\sum_{j=1}^{n_c} \frac{3\mu C_D Re}{4\rho_p d_p^2}(u_{p,i} - u_i)\dot{m}_p^j \Delta t^j \tag{5}$$

where $V_c$ is the volume of the discretized cell; $\dot{m}_p^j$ is the time rate of change of particle mass in $j$th trajectory passing through a discretized cell C out of $n_c$ number of total trajectories; Re is the Reynolds number; $\Delta t^j$ is the time required for a particle on $j$th trajectory to cross a cell; $C_D$ is the drag coefficient presented in Eq.

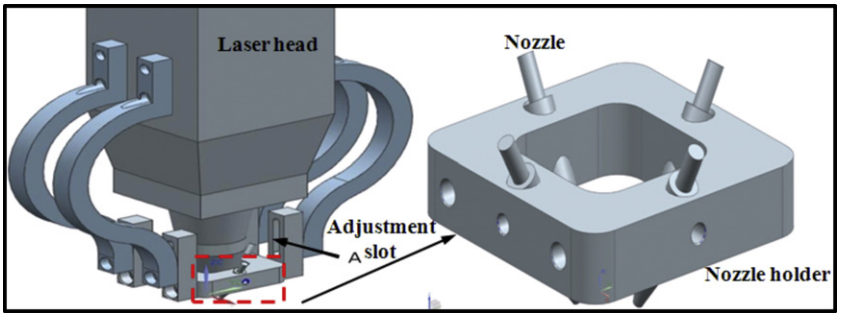


**Fig. 1.** A 3D model of the powder feeding head with a laser head.

(14). $u_{pi}$, $\rho_p$, and $d_p$ are the velocity in the $i$ direction, the density and the diameter of a particle, respectively. The density of NT-20, NT-60, NT-80 and WC powder is considered to be 8234 kg/m$^3$, 9557 kg/m$^3$, 10,444 kg/m$^3$, and 16,250 kg/m$^3$, respectively. In the current study, the size distribution of the particle is considered by using the Rosin–Rammler distribution. According to this relationship, the mass fraction of the particles with a diameter greater than $d$ is expressed as

$$F_d = \exp\left(-\left(\frac{d}{d_m}\right)^n\right) \tag{6}$$

here $d$ is the particle diameter, $d_m$ is the mean particle diameter, and $n$ is the measure of the spread of the particles. For the powders used in this study, the maximum and minimum diameters are chosen to be 50 μm and 150 μm based on the measurement and sieve analysis. While, the measured value of the mean particle diameter order is WC > NT-80 > NT-60 > NT-20.

An important issue is the variation in the shape of the powder particles. In a real case, not all of the powder particles are uniformly spherical but some are near-spherical and non-spherical. In order to incorporate this effect, a variable called the shape factor is used in the commercial code. This variable defines the degree of closeness of the particles to the spherical shape and is expressed as:

$$\varphi = \frac{s}{S} \tag{7}$$

where $s$ is the surface area of a sphere having the same volume as the particle, and $S$ is the actual surface area of the particle.

The powder flow during LBPD is turbulent in nature and causes velocity fluctuation; therefore, two more extra equations are required to solve the mass and momentum conservation equations in a time averaged manner. The most commonly used model to handle this situation is the standard $k$–$\varepsilon$ model in which the $k$ and $\varepsilon$ represents the turbulent kinetic energy and dissipation of kinetic energy, respectively.The conservation of the kinetic energy of turbulence is expressed as

$$\frac{\partial(\rho k u_i)}{\partial x_i} = \frac{\partial}{\partial x_j}\left[\left(\mu + \frac{\mu_t}{\sigma_k}\right)\frac{\partial k}{\partial x_j}\right] + G_k + G_b - \rho\varepsilon \tag{8}$$

The conservation of the dissipation of kinetic energy of turbulence is:

$$\frac{\partial(\rho\varepsilon u_i)}{\partial x_i} = \frac{\partial}{\partial x_j}\left[\left(\mu + \frac{\mu_t}{\sigma_k}\right)\frac{\partial \varepsilon}{\partial x_j}\right] + C_{1\varepsilon}\frac{\varepsilon}{k}(G_k + C_{3\varepsilon}G_b) - C_{2\varepsilon}\rho\frac{\varepsilon^2}{k} \tag{9}$$

$$G_k = \mu_t\left(\frac{\partial u_j}{\partial x_i} + \frac{\partial u_i}{\partial x_j}\right)\frac{\partial u_i}{\partial x_j} \tag{10}$$

$$G_b = -g_i\frac{\mu_t}{\rho Pr_t}\frac{\partial \rho}{\partial x_i} \tag{11}$$

where $G_k$ is the kinetic energy generation rate due to the average velocity gradient, $G_b$ is the turbulence energy generation due to buoyancy force, $Pr_t$ is the turbulence Prandtl number, and the other empirical constants are $\sigma_k = 1.0$, $\sigma_\varepsilon = 1.3$, $C_{1\varepsilon} = 1.44$, $C_{2\varepsilon} = 1.92$, and $C_\mu = 0.09$ (Fluent 6.3, 2006). The constant $C_{3\varepsilon}$ is 1.0 (Fluent 6.3, 2006) when the gas stream direction is approximately parallel to the direction of gravity.

### 2.2. Modeling of powder particles

A force balance method is used to model the powder particles

$$\frac{du_p}{dt} = \frac{18\mu}{\rho d_p^2}\frac{C_D Re}{24}(u - u_p) + \frac{g(\rho_p - \rho)}{\rho_p} \tag{12}$$

where $\mu$ is the fluid phase dynamic viscosity, and Re is the Reynolds number expressed as

$$Re = \frac{\rho d_p\left|u - u_p\right|}{\mu} \tag{13}$$

where $\rho_p$, $d_p$, $u_p$ are the density, diameter, and velocity of the individual particles, respectively. The drag coefficient $C_D$, with four empirical constants to incorporate the non-spherical nature of the particles is given as (Fluent 6.3, 2006),

$$C_D = \frac{24}{Re}(1 + a_1 Re^{a_2}) + \frac{a_3 Re}{a_4 + Re} \tag{14}$$

$$a_1 = \exp(2.3288 - 6.4581\varphi + 2.44\varphi^2) \tag{15}$$

$$a_2 = 0.0964 + 0.5565\varphi \tag{16}$$

$$a_3 = \exp(4.905 - 13.8944\varphi + 18.422\varphi^2 - 10.2599\varphi^3) \tag{17}$$

$$a_4 = \exp(1.4681 - 12.2584\varphi - 20.7322\varphi^2 + 15.8855\varphi^3) \tag{18}$$

where $\varphi$ is the shape factor.

The commercial computational fluid dynamics (CFD) code, FLUENT, handles the turbulent dispersion of particles by integrating the trajectory equations for individual particles using the instantaneous fluid velocity, $u_i^g + u_i'(t)$, along the particle path during the integration process. A discrete phase random walk or "eddy lifetime" model is employed to incorporate the turbulent fluctuations of the velocity components, $u_i'$, over a eddy time scale $T_L$:

$$u_i' = \varsigma\sqrt{\frac{2k}{3}} \tag{19}$$

$$T_L \approx 2C_L\frac{k}{\varepsilon} \tag{20}$$

where $\zeta$ is the normally distributed random number for all three directions stems from the isotropic turbulence assumption, and $C_L$ is the time scale constant (Tabernero et al., 2010). The particle eddy crossing time, $t_{cross}$, is presented as

$$t_{cross} = -\tau_p \ln\left[1 - \left(\frac{L_e}{\tau_p\left|u_i^g - u_i^p\right|}\right)\right] \tag{21}$$

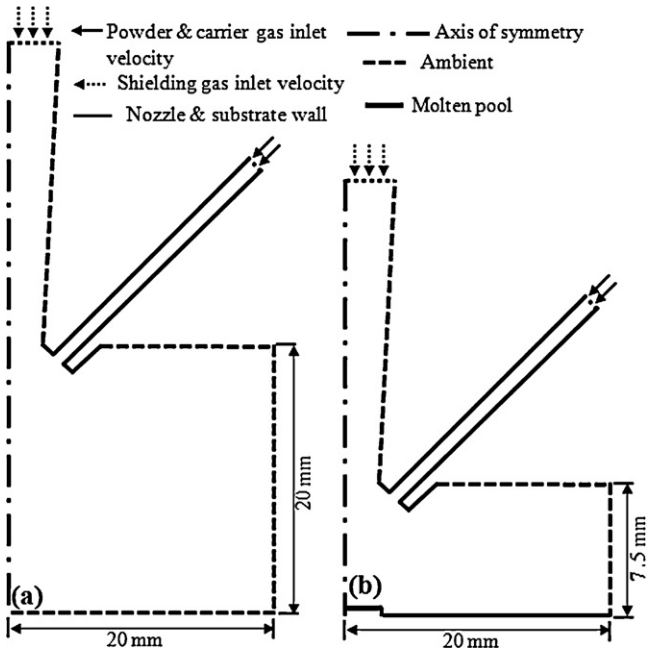


**Fig. 2.** Boundary conditions: (a) free flow; (b) with substrate (Zekovic et al., 2007).

here $\tau_p$ is the particle relaxation time, $L_e$ is the eddy length scale, and $\left|u_i^g - u_i^p\right|$ is the magnitude of the relative velocity. The particle interacts with the fluid eddy over the interaction time. When the eddy lifetime is reached, a new value of the instantaneous velocity is obtained by applying a new value of $\zeta$ in Eq. (19) (Tabernero et al., 2010).

### 2.3. Incorporation of the particles rebound from the nozzle solid walls

As the powder particle moves with the gas, it collides on the interior solid walls of the nozzle and then bounces. The bouncing of the particle depends on its material, the material of the nozzle wall, the particle morphology and wall roughness. The bouncing particle is composed of both normal velocity $(V_{pn})_b$ and tangential velocity $(V_{pt})_b$ that can be expressed in terms of the velocity of the colliding particle as $(V_{pn})_b = -k_n(V_{pn})_c$ and $(V_{pt})_b = k_\tau(V_{pt})_c$. The coefficients $k_n$ and $k_\tau$ define the degree of change in the velocity after the collision that is called the restitution coefficient. At $k_n \approx 1$, the collision of particle and wall is elastic, while the $k_n \ll 1$ non-elastic (Kovalev et al., 2010).

### 2.4. Boundary conditions and assumptions

Two different calculation domains are used to study the powder flow characteristics during the LBPD process. In the first case, a free flow mesh is used in which the presence of substrate is not considered. While in the second case, the substrate is included in order to mimic the real scenario of the LBPD process. The geometrical modeling, meshing, and specification of boundary types are performed in the GAMBIT-6.3 software. The software also offers an element quality test that is used in the current study to test the quality of the mesh. Fig. 2 shows the dimensions and boundary conditions in a 2D sectional view of the 3D calculation domain. The specified boundary conditions are represented as different lines in Fig. 2. The axis line, solid line and dashed line represent the axis of symmetry, rebounding wall, and ambient boundary condition, respectively. Similarly, the solid line and dotted line with the one-sided arrow-head indicate the powder–gas mixture and shielding gas inlet velocity boundary condition, respectively. Also, a thick solid line represents the width of the molten pool that is obtained in real-time from the digital images captured using the vision system as presented by Labudovic et al., 2003.

Following are the different boundary conditions considered in the current study based on Zekovic et al. (2007).

- A viscous, compressible, and steady-state gas flow is considered.
- At the shielding gas nozzle inlet and powder–gas mixture nozzle inlet, a constant velocity is applied perpendicular to the inlet surface.
- The discrete phase model is based on a force balance for each particle. In this model, only drag, inertial, and gravity forces are considered.
- The volume fraction of particles in the carrier gas flow is very small (<10%); hence, the influence of the particles on the gas flow as well as collisions of particles to each other are ignored.
- The interaction between the particle and laser irradiation is ignored.

The sensitivity of the grid size on the interested output variables such as discrete phase concentration, and particle and gas velocity contours are analyzed to optimize the size of the grid. The optimized mesh of the calculation domain for different cases is presented in Fig. 3.

## 3. Experimental study

The experimental setup consists of four radially symmetrical coaxial nozzles. Gas atomized, near-spherical as well as non-spherical, Ni–WC powder and WC powder of the mesh size −140/+325 supplied by Carpenter™ are used in this study. In addition, nano-sized WC powder in mass fraction from 0 to 10% is pre-mixed with the micron-sized powders using a ball mill, also used in this study. In order to feed the pre-mixed micro- and nano-sized powders with an ease the externally attached vibrators at the powder feeding system are used. For an accurate simulation of the particle characteristics, the size distributions of the different types of powders are studied by scanning electron microscope (SEM) and sieve analysis. The SEM micrographs of the used powders are presented in Fig. 4a–d, and the comparison of size distribution of the measured and assumed Rosin–Rammler particle distribution of the NT-20 powder is shown in Fig. 4e.

In order to validate the developed model, powder flow characteristics such as the powder particles stream structure, stand-off distance, powder spot size at the stand-off distance, and the velocity of powder particles, are measured using three different imaging techniques.

In the first imaging technique, the powder stream is illuminated by a 532-nm wavelength green laser, and a CCD camera at 30 frames per second is used to capture the illuminated powder stream. The evaluation window size is set as 15 mm in height and 15 mm in width. The schematic of experimental setup is shown in Fig. 5a.

In the second imaging technique, the transverse section of the powder stream at the different stand-off distances is captured to locate the maximum concentration spot and its diameter from the nozzles tips. The measurement window size of the each figure is maintained at a 12.7 mm in height and 12.7 mm in width. Based on the trial experiments it was concluded that the selected window size was large enough to monitor the flow behavior of the powder and; as such was opted in the current study. The components of the measurement system are a diode laser light source (Prophotonix™) with a 658-nm in wavelength and a line generating module, a mirror that is placed at 45° with respect to the CNC

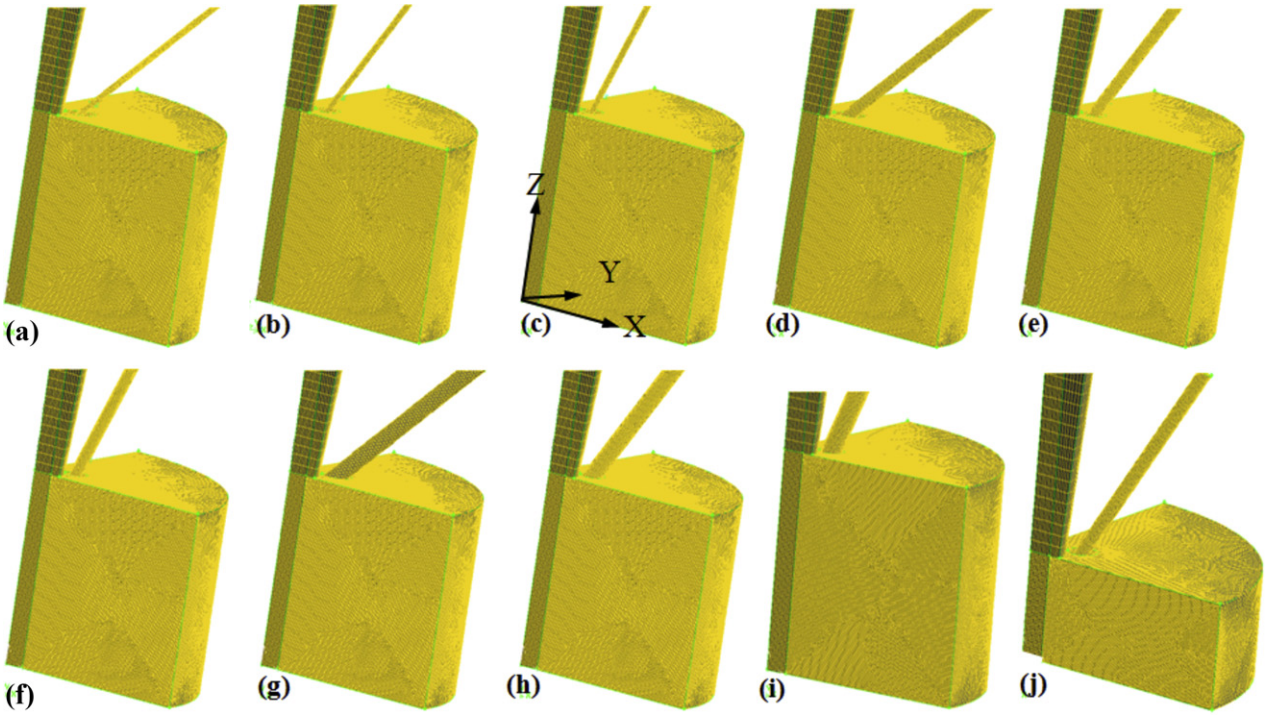


**Fig. 3.** Meshed calculation domain: (a)–(c) nozzle diameter 0.6 mm and nozzle angle 45°, 60°, and 70, respectively; (d)–(f) nozzle diameter 1.2 mm and nozzle angle 45°, 60°, and 70°, respectively;(g)–(i) nozzle diameter 1.8 mm and nozzle angle 45°, 60°, and 70°, respectively; (j) including substrate with nozzle diameter 1.2 mm and nozzle angle 60°.

table, and a CCD camera. A 200-μm thick sheet of laser light with uniform distribution is allowed to pass through the powder stream and the images are captured using a CCD camera at 10 frames per second. The schematic of experimental setup is displayed in Fig. 5b.

In the third imaging technique, an approximate method is followed to measure the velocity of the powder particle at the nozzle exit (Fig. 6a) based on the trace length of the particle. In this method, a high speed CCD camera with the exposure time set at 0.1 ms (shutter speed) and the powder stream illuminated by a green laser of 532 nm wavelength are used. The powder stream velocity measurements are made at the nozzle exit within the evaluation window size of 9.14 mm in height and 3.97 mm in width. The velocity of the powder particle ($V_p$) can be expressed in terms of the leading and trailing point coordinates of the captured trace of a single particle (trace length) at a particular time instant over the shutter speed of 0.1 ms as

$$V_p = \frac{\sqrt{(X_2 - X_1)^2 + (Z_1 - Z_2)^2}}{0.0001} \tag{22}$$

where $X_2, Z_2$ are the coordinates of the leading point of the powder particle trace at a particular time instant, and $X_1$, $Z_1$ are the coordinates of the trailing point of the same powder particle trace at the same time instant. Fig. 6b shows the schematic of the velocity measurement scheme. For example, based on the coordinates of the leading point L1 (2.1, 5.9) and the trailing point T1 (1.6, 7.1) of the particle trace (see Fig. 6b) and from the known camera shutter

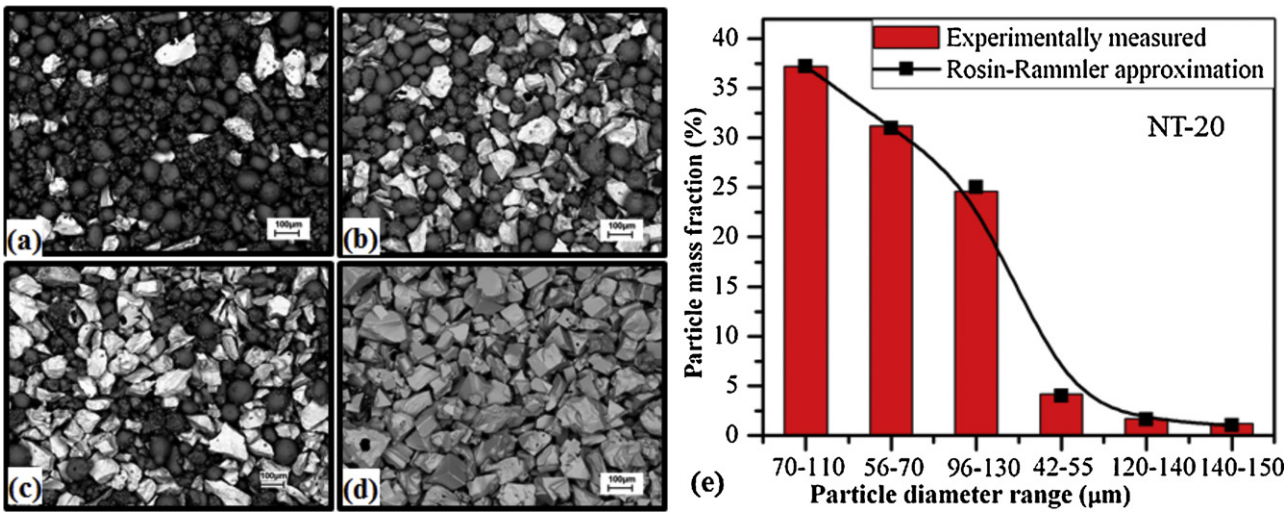


**Fig. 4.** Powder distribution: (a)–(d) SEM micrographs of the NT-20, NT-60, NT-80 and WC powder, respectively; (e) comparison between measured and assumed Rosin–Rammler particle size distribution of NT-20 powder.

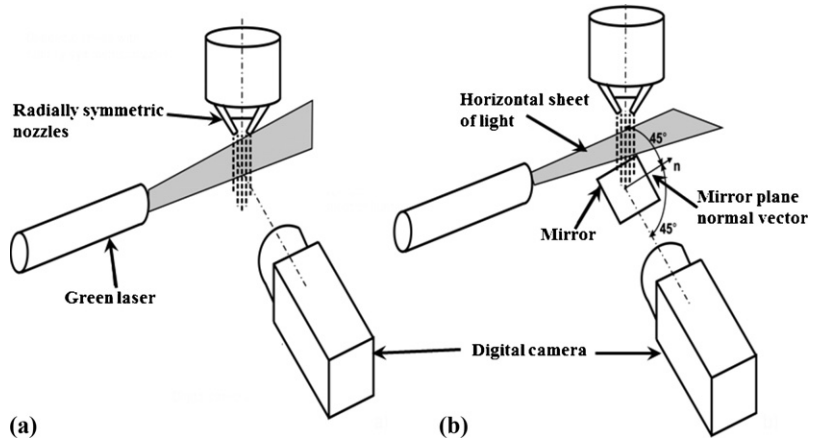


**Fig. 5.** Schematic of powder flow visualization set-ups: (a) stand-off distance; (b) powder concentration diameter and stand-off distance (Zekovic et al., 2007).

speed (0.1 ms), the velocity of the powder particle can be estimated using Eq. (22). Further, it is realized that all the particles are not traveling at the same speed due to the difference in shape and density; i.e., there exists a difference in the trace length of the particle. More importantly, the difference in trace length can also occur when the particles trace are not parallel to two-dimensional observing plane. In order to confirm the particle traces are parallel with the camera (view plane), particle trace with uniform brightness is considered for the velocity measurement. Also, in order to avoid the measurement error, a large number of images (100 images) were captured at different time instants and the average velocity is considered from the trace length over shutter speed. Using this procedure, the velocity of the powder particle is calculated, and the values are used for the validation of the numerical model.

### 3.1. Experimental results

#### 3.1.1. Measurement of stand-off distance

Table 1 presents a summary of the experiments performed to visualize the flow of Ni–WC powder with different mass fractions of the micro and nano-sized WC powder and monolithic micro-sized WC powder at three different carrier gas flow rates: $3.94 \times 10^{-5}$, $9.84 \times 10^{-5}$, and $15.74 \times 10^{-5}$ $m^3/s$. The first and second rows of the table represent the powder flow images of NT-20 and micro WC, respectively delivered from a single powder feeder. To further investigate the effect of mixing the powder of different types of material groups on the flow characteristics, another set of experiments is performed using two powder feeders (Valant and Kovacevic, 2006). Third row of the table displays powder flow images of the equal mass fraction of NT-20 and NT-80 powders, each premixed with 5% of nano-sized WC. Fourth row of the table shows the powder flow images of the equal mass fraction of NT-60 (premixed with 10% nano-sized WC) and micro-sized WC powder. In all of these cases, the powder flow rate is maintained at 0.08 g/s. The following qualitative analysis of the powder flow is based on the assumption that the luminance intensity is directly proportional to the concentration of the particle. It is evident from the images that the stream starts to expand as soon as it exits from the nozzle tip and continues to expand. The stand-off distance can be easily read from the scale. In general, the powder particles' stream structure after the nozzle exit can be divided into three distinct regimes: converging stream, stream waist, and diverging stream which is stated in the literature (Wen et al., 2009). Further, in the radial direction of the powder stream, an inner core with higher powder concentration and a relatively lower powder concentration outer shell can be observed. This also represents a typical Gaussian distribution of powder stream that is reported in the literature (Lin, 2000). A comparison of images on the first row that corresponds to the NT-20 powder delineates that an increase in gas flow rate significantly affects the powder concentration. This could be due to the fact that for an increase in carrier gas flow rate, the powder stream released from an individual nozzle spreads or diverges before the gathering spot of the powder streams, subsequently leading to less powder concentration. Also, it is worthwhile to note that this divergence causes the clouding of the powder stream before the actual converging spot of all four powder streams. The micro-sized WC powder shows a reverse trend from $3.94 \times 10^{-5}$ to $9.84 \times 10^{-5}$ $m^3/s$. This can be attributed to the fact that the negative pressure at the suction orifice inside the powder feeder chamber is not sufficient to overcome the mass of the WC powder at the $3.94 \times 10^{-5}$ $m^3/s$ carrier gas flow rate. This causes a lesser powder flow rate. Further, it can be observed that the collision of the particles at the converging spot and the subsequent loss of momentum results in the particles falling immediately underneath the stream waist. Further, the WC powder suffers from instability in flow at a higher carrier gas flow rate as compared to the other powders. It can be surmised that the combination of non-spherical shape and high density results in an increased collision dynamics of the particles in the nozzle wall as well as in the gathering spot, causing instability in the flow.

From the third and fourth rows (Table 1) a discernible increase in powder stream divergence as well as the powder cloud in the background can be seen at a higher carrier gas flow rate. Since, the nano-sized particle is lighter than the micro-sized particle, an

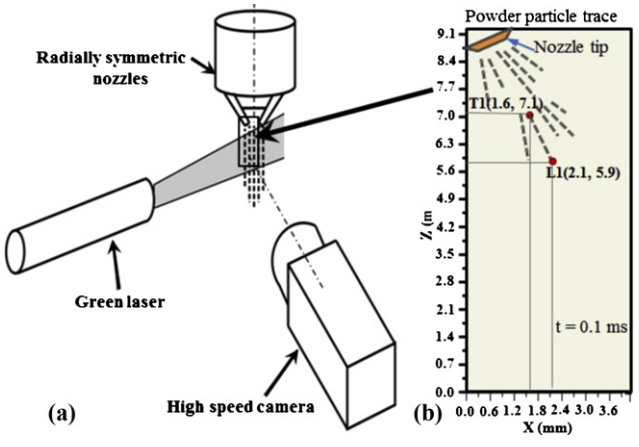


**Fig. 6.** Schematic of velocity measurement (a) and velocity measurement scheme (b).

**Table 1**
Multi-material powder delivery from single and two powder feeders.

| Powder material | Carrier gas flow rate ($m^3/s$) | | |
|---|---|---|---|
| | $3.94 \times 10^{-5}$ | $9.84 \times 10^{-5}$ | $15.74 \times 10^{-5}$ |
| NT-20 | 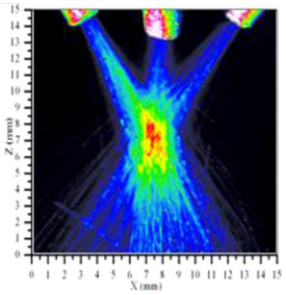 | 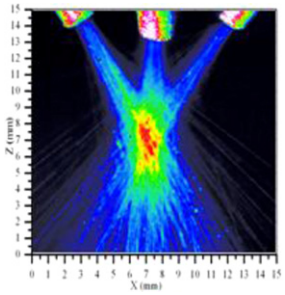 | 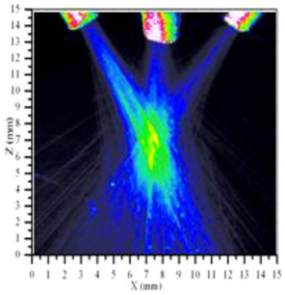 |
| WC | 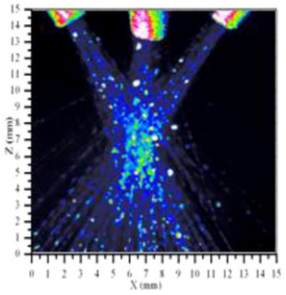 | 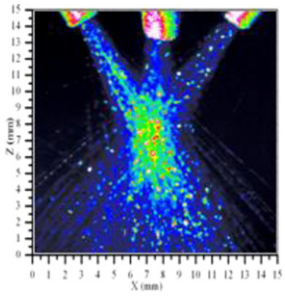 | 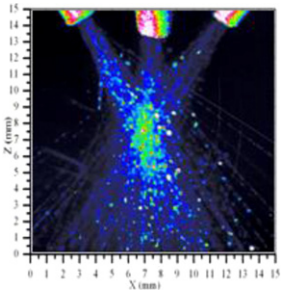 |
| NT-20 pre-mixed with 5% nano WC + NT-80 pre-mixed with 5% nano WC | 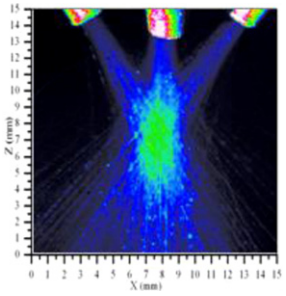 | 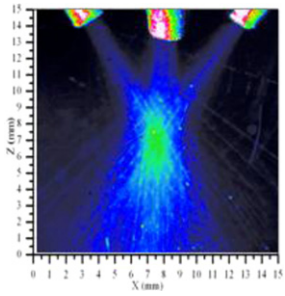 | 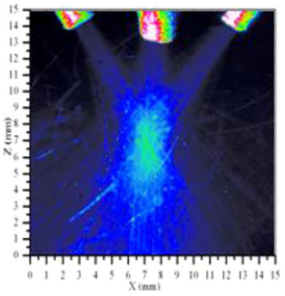 |
| NT-60 pre-mixed with 10% nano WC + micro WC | PF1 = $3.94 \times 10^{-5}$ PF2 = $3.94 \times 10^{-5}$ 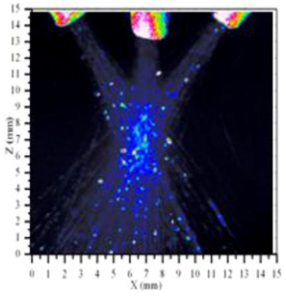 | PF1 = $5.9 \times 10^{-5}$ PF2 = $3.9 \times 10^{-5}$ 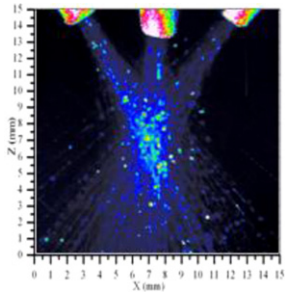 | PF1 = $7.84 \times 10^{-5}$ PF2 = $5.95 \times 10^{-5}$ 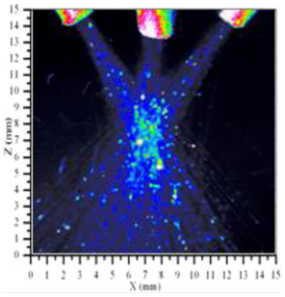 |

PF1, powder feeder#1; PF2, powder feeder#2.

increase in the gas flow rate results in the escape of nano particles from the powder stream. This can lead to the scarcity of nano WC in the deposited material as compared to the pre-mixed powder composition. In order to maintain the pre-mixed or on-the-fly mixed multi-material powder composition in the deposited material, a suitable choice of carrier gas flow rate needs to be identified. To demonstrate the significant change in the flow pattern for a change in the carrier gas flow rate, a smaller increment of carrier gas flow rate is used in the same combination of material in the 4th row of Table 1. Evidently, there exists a significant variation in the powder flow pattern even for a small variation in the carrier gas flow rate.

It is understood from the experiments that the instability in flow of multi-material powder can be minimized by optimizing the influencing parameters. More importantly, the carrier gas flow rate can be adjusted to compensate for the instability of the conditions that stem from the particle mass and its morphology.

### 3.1.2. Powder stream intensity distribution

Fig. 7 represents the luminance intensity distribution of the NT-60 powder stream cross-sections at four distances from the tips of nozzles such as: $Z = 4$ mm, $Z = 6$ mm, $Z = 7$ mm, and $Z = 8$mm plane. The powder flow rate is maintained at 0.08 g/s in all these images except in Fig. 7b1. In order to study the influence of the powder flow rate on the stand-off distance, the powder flow rate is increased to 0.5 g/s, and the image corresponding to this condition is shown in Fig. 7b1. It can be seen that the maximum powder concentration with a near-circular shaped powder stream occurs at $Z = 8$ mm. An evident increase in maximum concentration and change in shape

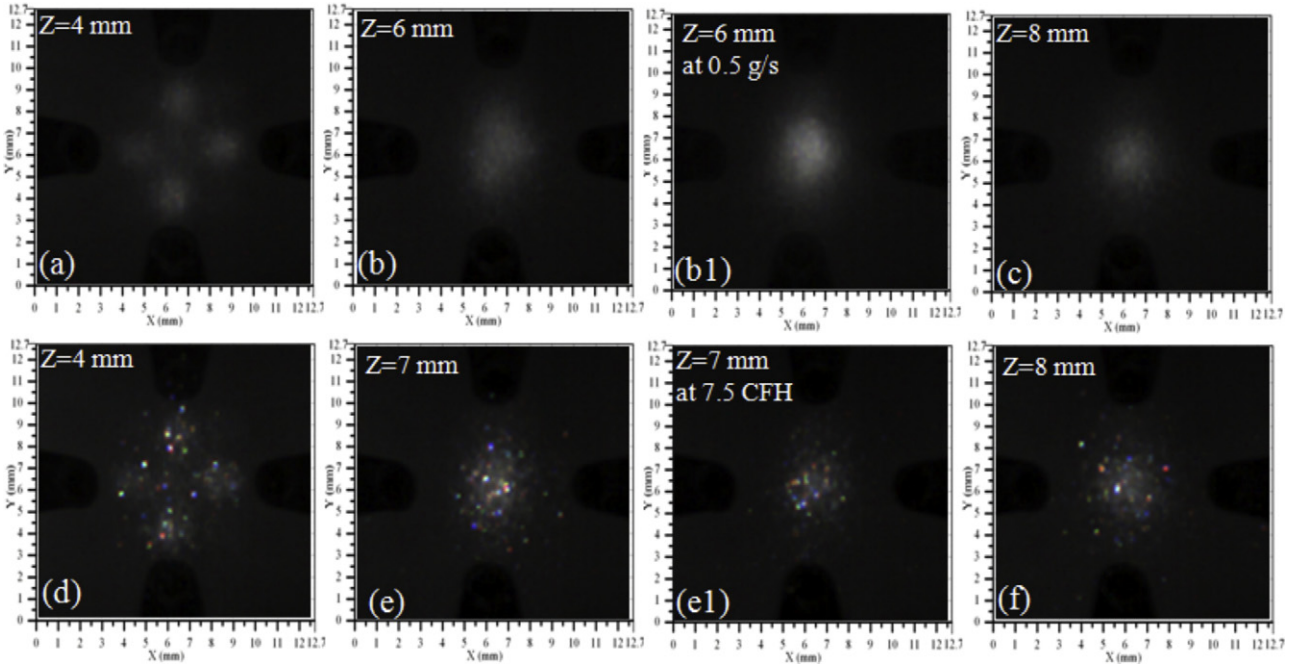


**Fig. 7.** Powder stream luminance intensity images at different stand-off distances (a)–(c) corresponds to NT-60 at $Z = 4$ mm, at $Z = 6$ mm and at $Z = 8$ mm, respectively (b1) corresponds to NT-60 at $Z = 6$ mm for a powder flow rate of 0.5 g/s; (d)–(f) corresponds to WC at $Z = 4$ mm, at $Z = 7$ mm and at $Z = 8$ mm, respectively (e1) $Z = 7$ mm at $5.9 \times 10^{-5}$ m$^3$/s of carrier gas flow rate.

can be seen for an increase in the powder flow rate at a stand-off distance of 6 mm (see Fig. 7b and b1). This clearly indicates that a very high powder flow rate can cause a premature gathering of the powder. A closer examination of these images reveals that the maximum concentration occurs at the center and decreases toward the radial direction confirming a typical Gaussian powder distribution.

Fig. 7d–f shows the luminance intensity distribution of the WC powder stream at different stand-off distances ($Z$) at a powder flow rate of 0.08 g/s. The carrier gas flow rate is maintained at $9.84 \times 10^{-5}$ m$^3$/s in all these images except in Fig. 7e1. In order to demonstrate the influence of the carrier gas flow rate on the stand-off distance, the carrier gas flow rate is decreased to $5.9 \times 10^{-5}$ m$^3$/s and the corresponding image to this condition is shown in Fig. 7e1. It can be observed that the luminance intensity of the WC particles is higher than the Ni-based powder due to the presence of the highly reflective surface of the WC powder particles. A pronounced scattering of the WC particles indicates the unstable flow condition. The maximum powder concentration with a near-circular shaped powder stream occurs at both $Z = 7$ mm, and $Z = 8$ mm. Notably, a reduction in scattering can be seen for a decrease in the powder flow rate at a stand-off distance of $Z = 7$ mm (see Fig. 7e and e1). The approximate diameter of the powder stream at the stand-off distance is 2.5 mm, and can be directly read from the fixed scale.

In general, a marginal variation in the stand-off distance is observed between the Ni–WC powders and WC powder. This may be due to the non-spherical shape, particle properties, and the collision of particles at the nozzle wall (Kovalev et al., 2010).

### 3.1.3. Particles velocity measurement

As mentioned before the velocity of the powder particle is an important variable that influences the powder flow characteristics, and the different methods are reported in the literature to measure the velocity of the particle (Zhang et al., 2009; Wen et al., 2009; Kovalev et al., 2010). However, in the current study, an approximate method is used to measure the velocity of the particle. Fig. 8a shows the powder delivery images of the NT-20 at the nozzle exit for a powder flow rate and carrier gas flow rate of 0.08 g/s and $5.9 \times 10^{-5}$ m$^3$/s, respectively. The time interval between each image is 0.1 ms. The particle trace length "L" of NT-20 powder can be read from Fig. 8. For example, the velocity of the NT-20 powder particle trace length, L, is measured to be 10.77 m/s (see Fig. 8a) based on the coordinates of L1 (1.1, 6.85) and T1 (0.7, 7.85). A closer examination of the instantaneous images shows that not all of the powder particles traces are of same length that shows that they are traveling at different velocities; there exists a difference in transportation behavior in terms of velocity and divergence of the stream that could be due to the difference in size, morphology and collision dynamics of the particles at the nozzle wall (Kovalev et al., 2010).

Similarly, NT-80 and WC powder particles traces were captured and presented in Fig. 8b and c, respectively. A lower powder flow rate of 0.06 g/s is chosen to clearly visualize the individual powder particle trace whereas; the gas flow rate is maintained as $5.9 \times 10^{-5}$ m$^3$/s. Following the same procedure demonstrated in

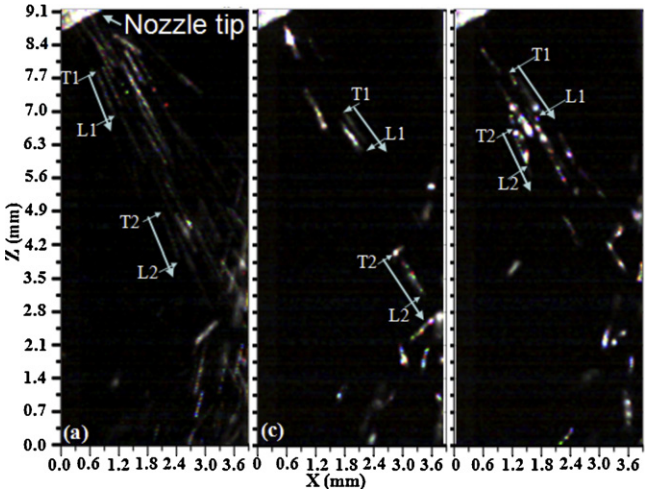


**Fig. 8.** Powder delivery images captured at the nozzle exit: (a) NT-20; (b) NT-80; (c) WC.

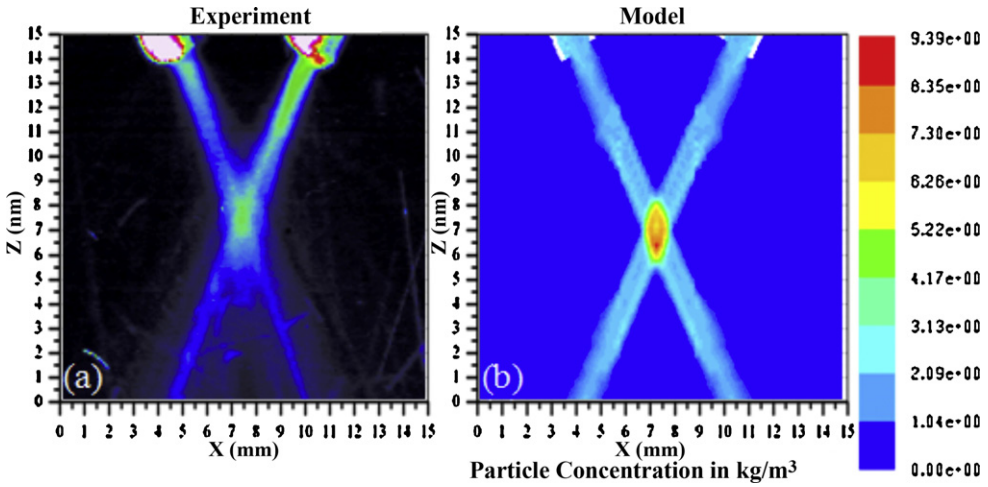


**Fig. 9.** NT-20 powder stand-off distance comparison between experimental and numerical results at a carrier gas flow rate of $3.94 \times 10^{-5}$ m$^3$/s and a powder flow rate of 0.06 g/s: (a) experiment; (b) calculated results in $y$–$z$ plane.

the case of NT-20 powder the trace length of any NT-80 and WC powder particle (Fig. 8b and c) can be measured from the coordinates of the leading point, and trailing point. For instance, the measured velocity of the NT-80 powder from Fig. 8b is 8.25 m/s. In general, the measurements have showed that the velocity of the fastest particle is approximately two folds higher than the velocity of the slowest particle. Also, it is observed that the heavier WC particles have, as expected, lower velocities and that the effect of the higher density is to flatten the carrier gas velocity profile. From the experiments it is identified that at the carrier gas flow rate of $15.74 \times 10^{-5}$ m$^3$/s, the velocity of the powder particle can exceed a value of 30 m/s.

In summary, the powder particle stream structure, concentration and velocity are predominantly influenced by the gas flow rate. The powder flow rate and the particle properties also show a significant influence on the powder flow characteristics.

### 3.2. Numerical results and discussion

The numerical model for a coaxial powder flow is developed based on the formulation presented in Section 2. Firstly, a check on the validity of the computational procedure is obtained from the experimental measurements of the stand-off distance, spot diameter, and particles stream velocity, using different photographic techniques. Further, the validated model is employed to study the effect of nozzle angle, nozzle diameter, powder particle morphology and property, powder particle collision behavior at the interior solid walls of the nozzle and gas flow rate on the interested output variables such as powder concentration and its velocity and powder spot size at different stand-off positions.

#### 3.2.1. Validation of numerical model

Fig. 9 shows the comparison between the experimental and numerical results in terms of powder stream structure and stand-off distance. For this case, the NT-20 powder is considered at a powder flow rate of 0.06 g/s and gas flow rate of $3.94 \times 10^{-5}$ m$^3$/s. The stand-off distance of the powder stream from the nozzle tip can be directly read from the fixed scales on the images obtained by experimental and numerical results, and the values are 7.5 mm and 8 mm, respectively. A closer observation of the numerical and experimental results indicates that powder stream diverges as soon as it exits from the nozzle tip. A good agreement between the results confirms that the model is capable of predicting the powder flow behavior during the coaxial powder feeding of the LBPD process.

A comparison of experimental (left) and numerical (right) results of the NT-20 powder stream convergence from the nozzle tip at the stand-off distances at $Z = 4$ mm, $Z = 7$ mm, and $Z = 8$ mm, are presented in Fig. 10. The carrier gas flow rate of $3.94 \times 10^{-5}$ m$^3$/s and powder flow rate of 0.08 g/s are considered. The following observations can be made from Fig. 10. First, the most concentrated powder stream occurs at the stand-off distance between 7 mm and 8 mm from the nozzle tip. Also, it can be seen from Fig. 10 that the area for the focused powder stream at 8 mm is smaller and more uniform than at 7 mm. This indicates that a combination of higher concentration and uniform stream diameter (based on the luminance intensity) occurs at 8 mm from the nozzle tip. The simulation results replicate the trends in the experimental results reasonably.

Fig. 11 presents the measured and simulated average velocity of NT-20, NT-80, and WC powders at the nozzle exit. The measured and simulated average velocity of the NT-20 powder is 10.1 m/s and 8.98 m/s, respectively. Similarly, the numerical results of all three powders are in a good agreement with the measured ones. It is observed that the order of the average velocity of powder is NT-20 > NT-80 > WC. This result could be related to the shape factor of the WC particle and its weight. It can be inferred from Fig. 11 that the particle velocity is in descending order from NT-20 through WC. In other words, it may be stated that the lighter the particles, the higher the velocity.

#### 3.2.2. Quantitative study on powder and gas flow behavior

Fig. 12 shows the effect of different nozzle angles on the maximum powder concentration and its structure. It can be stated that an increase in the nozzle angle leads to a decrease in the maximum powder concentration. This could be due to the fact that continuous increase in the divergence of the powder stream from the nozzle exit subsequently causes a decrease in the peak value of the maximum concentration of powder. It can be noticed from the particle concentration profile that an increase in the nozzle angle leads to the transition in the shape of the powder stream from near circular at lower angle to elliptical at a higher angle. Hence, it can be concluded that a higher nozzle angle can increase the laser powder particle interaction time. This in turns can enhance the particles preheating temperature before it reaches the laser formed molten pool at the substrate. Conversely, a larger interaction time can increase the shadowing effect, the attenuation of laser by powder cloud. It is reported in the literature (Wen et al., 2009) that the powder particles reach a maximum temperature of 1056 K at

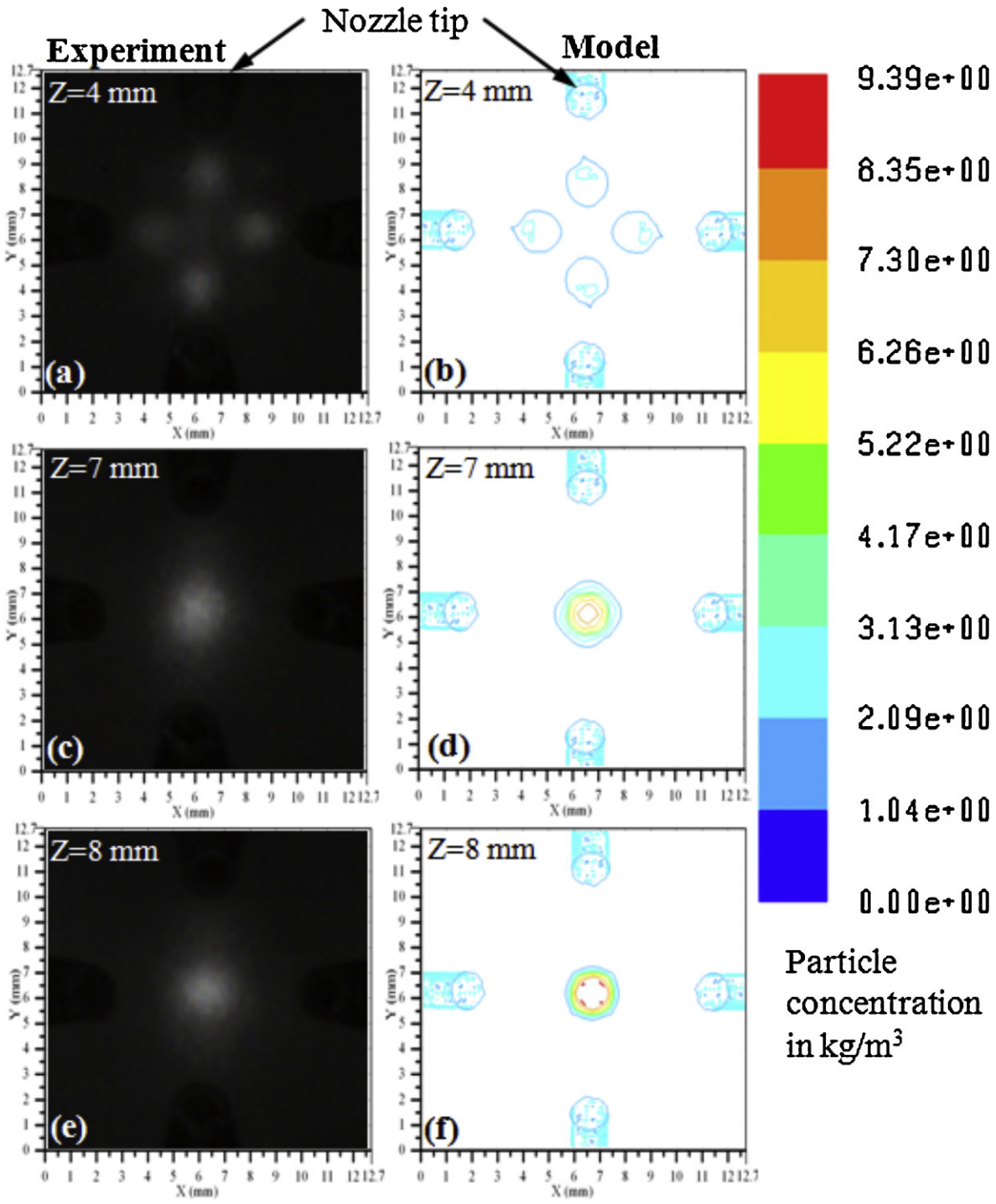


**Fig. 10.** A comparison between experimental and numerical results of NT-20 powder stream pattern at different cross-sections for a carrier gas flow rate of $3.94 \times 10^{-5}$ $m^3/s$ and powder flow rate of 0.08 g/s; (a) and (b) experimental and numerical results at $Z = 4$ mm from the nozzle tip; (c) and (d) experimental and numerical results at $Z = 7$ mm from the nozzle tip; (e) and (f) experimental and numerical results at $Z = 8$ mm from the nozzle tip.

a stand-off distance of 10 mm (Laser power = 300 W, beam diameter = 1.5 mm). Hence, an appropriate choice of nozzle angle for the specific material is essential. More importantly, in the case of multi-material coaxial powder flow, a longer interaction time can cause evaporation of the low melting particle and can deplete a specific element in the deposited layer as compared to the injected powder. For example, in the present case, having a longer time available for the particle to interact with the laser may lead to excessive heating of the WC particles. Consequently, this interaction can affect the dissolution level of WC (ceramic) in the Ni matrix.

The results concerning the carrier gas flow rate effect on the particles concentration for two different types of powders with substrate (at a stand-off distance of 7.5 mm) is illustrated in Fig. 13. The powder flow rate is kept at a constant value of 0.08 g/s for all these simulations. Three important variations can be noticed between the powder concentration profile corresponding to the case without substrate (free-flow) and with substrate. Evidently, the presence of substrate significantly changes the particle distribution in the radial direction and the maximum particle concentration; i.e., both the width of the concentration as well as

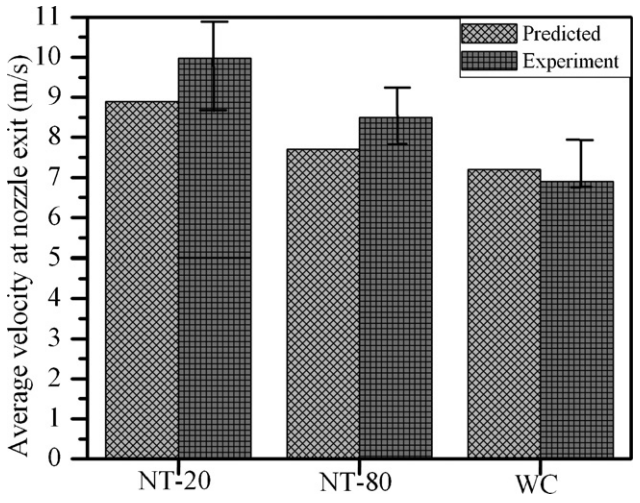


**Fig. 11.** Measured and predicted values of average velocity of the powder particles stream for NT-20, NT-80 and WC powders at a powder flow rate of 0.08 g/s and carrier gas flow rate of $3.94 \times 10^{-5}$ m$^3$/s.

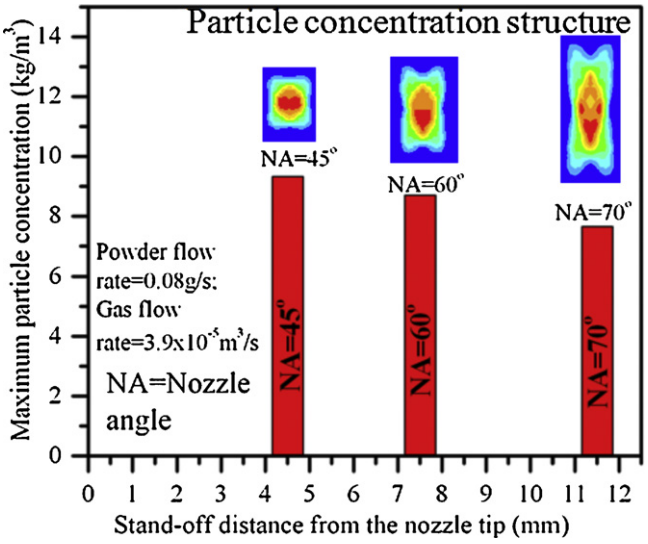


**Fig. 12.** Numerically simulated maximum powder concentration vs. stand-off distance from the nozzle tip for nozzle angles 45°, 60° and 70°.

the maximum concentration increases. Furthermore, the stand-off distance moves 1 mm upward as compared to the free-flow case. This could be due to the effect of the bouncing of particles from the substrate's top surface that in turn affects the powder flow characteristics. An increase in the gas flow rate drastically diminishes the particle concentration due to the decrease in the two-phase flow density. In order to numerically test the effect of mixing powders of varying properties, both NT-20 and WC of equal mass fraction (50% each) are separately injected from the nozzle inlet, and the results are presented in Fig. 13b. It is worthwhile to note that the powder concentration profile changes. In more detail, the Gaussian sharp peak has become relatively flat, and the flattening is more predominant toward an increased gas flow rate. This result indicates that the mixing of powders of different material properties significantly affects the concentration distribution.

In Fig. 14a, the particles rebound from the nozzle interior wall shows a strong influence on the particle concentration in the radial as well as axial directions. A complete elastic rebound ($K = 1$) increases the spread or the distribution of the powder concentration due to the divergence of the powder stream while the peak concentration drops considerably. The elastic rebound widens the powder distribution in radial direction. As the rebound approaches from elastic to plastic ($k < 1$), a more uniform powder distribution at the powder focal position occurs. The results indicate that the powder and nozzle material, powder morphology, and nozzle wall roughness (friction) can alter the powder flow characteristics (Kovalev et al., 2010).

Fig. 14b illustrates the velocity of carrier gas and powder particle at the gas flow rate of $3.94 \times 10^{-5}$ m$^3$/s and powder flow rate of 0.08 g/s. The flow pattern of the carrier gas velocity delineates that the gas velocity contour disperses immediately after the nozzle exit and drops down drastically before it reaches the substrate. The results concerning the effect of the shape factor of the powder particle and its diameter on the average velocity of the particle at the nozzle exit are shown in Fig. 15a and b, respectively. It can be summarized (Fig. 15a) that the lower the value of shape factor the higher the particle velocity. This result may be due to an increase in the drag force of the particle caused by a decrease in the value of the shape factor. Fig. 15b demonstrates that an increase in particle diameter has an adverse effect on the average velocity of the powder particle at the nozzle exit. The estimated velocity of WC is higher than the measured one which could be originated from the selection of the shape factor and the density used in the model. The NT-20, NT-60 and NT-80 powders composed of both spherical and non-spherical particles whereas, the WC particles are fully non-spherical as well the average particle size is larger than the other powder (see Fig. 4a–d).

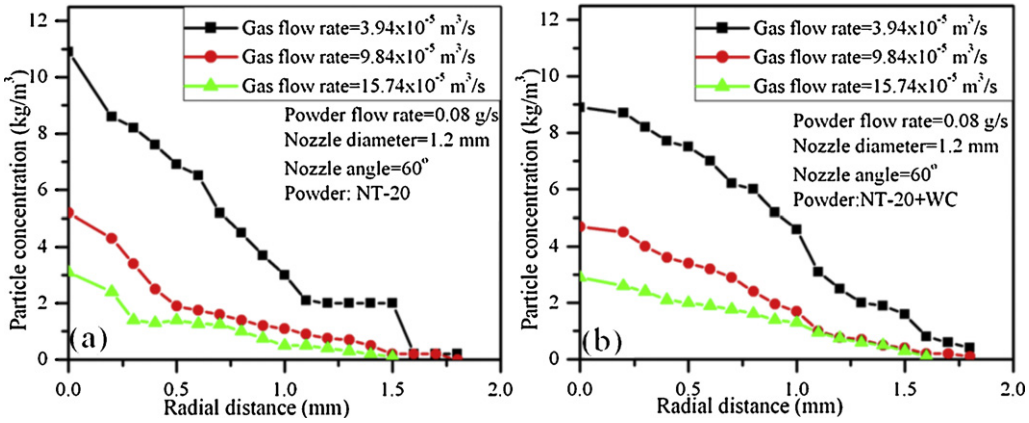


**Fig. 13.** Effect of carrier gas flow rate on the maximum powder concentration with substrate at a nozzle angle of 60° and at stand-off distance of 6.5 mm:(a) NT-20 powder; (b) NT-20 + WC powder.

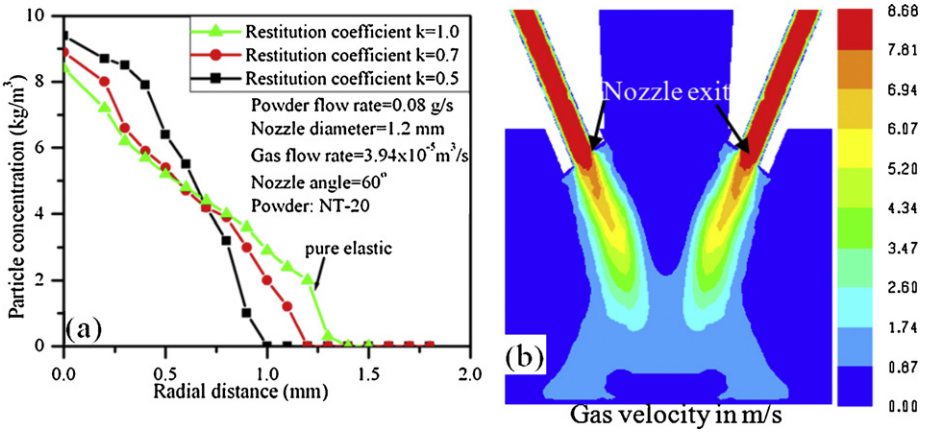


**Fig. 14.** (a) effect of particles rebounding on the concentration distribution at the stand-off distance of 6.5 mm; (b) carrier gas velocity contour at a gas flow rate of $3.94 \times 10^{-5}$ m$^3$/s.

### 3.3. Confirmatory experiments

To further investigate the applicability of the developed numerical model, a few conformal experiments are performed. From the simulation and the visualization aid it is found that a combination of stable and uniform multi-material powder flow with maximum concentration occurs at a stand-off distance of 6.5 mm from the nozzle tip and at the carrier gas flow rate of $5.9 \times 10^{-5}$ m$^3$/s irrespective of the range of powder flow rate used in this study.

Three layers of functionally graded composite material varying from NT-20 to NT-60 powder are deposited by the LBPD process. A 4 kW fiber laser of spot diameter of 3 mm at the substrate is used. The laser power of 725 W and the scanning speed of 8.33 mm/s are set to deposit ten tracks on each layer with a track length of 25 mm and the overlap ratio of 36%. An analytical expression based on the geometrical features of the single track is used to calculate the optimal overlap ratio as presented by Kai et al. (2007). Two different stand-off distances are used to demonstrate its effect on the deposition quality in terms of appearance. In the first case, the stand-off distance of 7.5 mm and carrier gas flow rate of $9.84 \times 10^{-5}$ m$^3$/s is opted. While in the second case, the stand-off distance is changed to 6.5 mm with the same carrier gas flow rate as previous one. In the third case, the carrier gas flow rate is changed to $5.9 \times 10^{-5}$ m$^3$/s by keeping the stand-off distance as 6.5 mm. Fig. 16a and b shows the difference in the surface quality of the deposited layers. In the first case, a wavy or irregular top surface with a total deposited height of 0.9 mm is obtained (see Fig. 16a1 and a2). In the second case, a slightly improved surface quality with a total deposited height of 1.8 mm is obtained (see Fig. 16b1 and b2). It is worthwhile to note that the deposits fabricated at a higher gas flow rate show a polished surface (Fig. 16a and b). Finally, in the third case (see Fig. 16c1 and c2) an even and smooth surface with a total deposit height of 2.64 mm is achieved. In summary, the validity of the numerical results demonstrates the predictive power of the model. Fig. 16d shows a smooth composition gradient from NT-20 to NT-60.

### 3.4. Conclusions

Based on the findings from the experimental study and the numerical model, the following conclusions are derived. The developed numerical model is utilized to improve the quantitative understanding of the powder flow characteristics of the multi-material coaxial powder flow during the LBPD process.

(a) A typical Gaussian powder distribution in both the radial and axial direction at the powder stream converging spot is observed. A higher value of carrier gas flow rate increases the divergence of the powder stream from the nozzle exit and subsequently reduces the powder concentration.
(b) A heavier non-spherical shaped WC particle suffers from instability in flow at the higher carrier gas flow rate as compared to the lighter spherical/near spherical shape particles. Further, a marginal increase in the stand-off distance is noticed in the case of WC powder.
(c) The average velocity of the tested powder particles is arranged as NT-20 > NT-80 > WC.

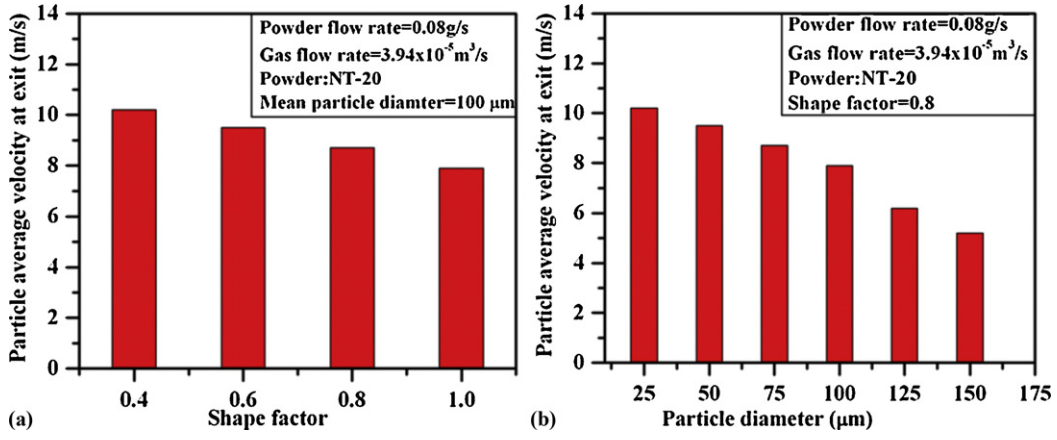


**Fig. 15.** (a) effect of shape factor of particle on average particle velocity at nozzle exit. (b) effect of particle diameter on average particle velocity at nozzle exit.

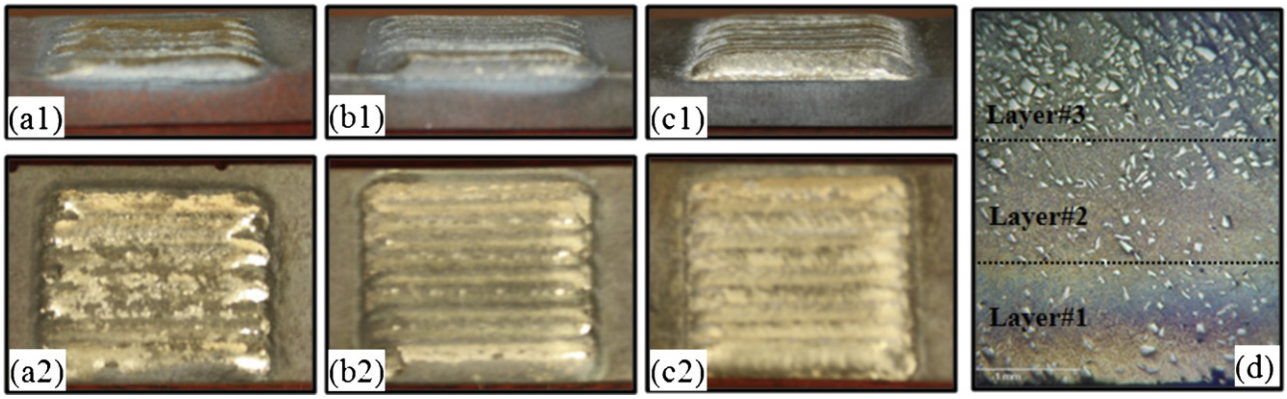


**Fig. 16.** Appearance and cross-section of the multi-track, three-layer from NT-20 to NT-60 deposits: (a1) and (a2) isometric view and top view of the deposit fabricated at the stand-off distance of 7.5 mm and the carrier gas flow rate of $9.84 \times 10^{-5}$ $m^3/s$; (b1) and (b2) isometric view and top view of the deposit fabricated for the stand-off distance of 6.5 mm and the carrier gas flow rate of $9.84 \times 10^{-5}$ $m^3/s$; (c1) and (c2) isometric view and top view of the deposit fabricated for the stand-off distance of 6.5 mm and the carrier gas flow rate of $5.9 \times 10^{-5}$ $m^3/s$; (d) cross-section corresponds to the (c1) and (c2).

(d) The change in nozzle angle is resulted in a longer powder stream waist and alters the shape of the powder stream waist from near circular at a lower angle to elliptical at a higher angle.
(e) The typical Gaussian distribution peak of the powder stream tends to be relatively flat in the multi-material powder flow, and the flattering is more predominant toward an increase in gas flow rate.
(f) The particles rebounding from the nozzle wall show a strong influence on the particle concentration in the radial as well as axial directions.
(g) The average velocity of the powder particles stream is influenced by the density, shape factor and diameter of the particle that plays a key role in stable powder flow.
(h) The confirmatory experiments delineate that the developed model can be used as a real design tool to achieve the desired powder flow characteristics of the multi-material powder based on the size of the laser beam at the substrate.

## Acknowledgement

This work was funded by NSF's Grant IIP-1034652.

## References

2006. Fluent 6.3 User Manual. Fluent Inc., Canonsburg, PA, USA.
Fu, Y., Loredo, A., Martin, B., Vannes, A.B., 2002. A theoretical model for laser and powder particles interaction during laser cladding. Journal of Materials Processing Technology 128, 106–112.
Huang, Y.L., Liang, G.Y., Su, J.Y., Li, J.G., 2005. Interaction between laser beam and powder stream in the process of laser cladding with powder feeding. Modelling and Simulation in Materials Science and Engineering 13, 47–56.
Huang, Y.L., Liu, J., Ma, N.H., Li, J.G., 2006. Three-dimensional analytical model on laser–powder interaction during laser cladding. Journal of Laser Applications 18, 42–46.
Kai, Z., Weijun, L., Xiaofeng, S., 2007. Research on the processing experiments of laser metal deposition. Optics and Laser Technology 39, 549–557.
Kovalev, O.B., Zaitsev, A.V., Novichenko, D., Smurov, I., 2010. Theoretical and experimental investigation of gas flows, powder transport and heating in coaxial laser direct metal deposition (DMD) process. Journal of Thermal Spray Technology 20, 465–478.
Labudovic, M., Hu, D., Kovacevic, R., 2003. A three dimensional model for direct laser metal powder deposition and rapid prototyping. Journal of Materials Science 38, 35–49.
Lin, J., Steen, W.M., 1998. Design characteristic and development of a nozzle for coaxial laser cladding. Journal of Laser Applications 10, 55–63.
Lin, J., 2000. Numerical simulation of the focused powder streams in coaxial laser cladding. Journal of Materials Processing Technology 105, 17–23.
Pan, H., Sparks, T., Thakar, Y.D., Liou, F., 2006. The investigation of gravity-driven metal powder flow in coaxial nozzle for laser-aided direct metal deposition process. Journal of Manufacturing Science and Engineering 128, 541–553.
Picasso, M., Marsden, C.F., Wagniere, J.-D., Frenk, A., Rappaz, M., 1994. Laser–powder–material interaction in the laser cladding process. Metallurgical Transactions B Process Metallurgy 25, 281–291.
Pinkerton, A.J., Li, L., 2004. Modelling powder concentration distribution from a coaxial deposition nozzle for laser-based rapid tooling. Journal of Manufacturing Science and Engineering Transactions ASME 126, 33–41.
Tabernero, I., Lamikiz, A., Ukar, E., Ĺopez de Lacalle, L.N., Angulo, C., Urbikain, G., 2010. Numerical simulation and experimental validation of powder flux distribution in coaxial laser cladding. Journal of Materials Processing Technology 210, 2125–2134.
Valant, M., Kovacevic, R., 2006. Powder delivery system and method. US Patent #7,045,738B1.
Weisheit, A., Backes, G., Stromeyer, R., Gasser, A., Wissenbach, K., Poprawe, R., 2001. Powder injection: the key to reconditioning and generating components using laser cladding. In: Proceedings of International Congress on Advanced materials and Processes, Materials Week, Munich, Germany.
Wen, S.Y., Shin, Y.C., Murthy, J.Y., Sojka, P.E., 2009. Modeling of coaxial powder flow for the laser direct deposition process. International Journal of Heat and Mass Transfer 52, 5867–5877.
Yang, N., 2009. Concentration model based on movement model of powder flow in coaxial laser cladding. Optics and Laser Technology 41, 94–98.
Zhang, F., Chen, J., Tan, H., Lin, X., Huang, W., 2009. Composition control for laser solid forming from blended elemental powders. Optics and Laser Technology 41, 601–607.
Zekovic, S., Dwivedi, R., Kovacevic, R., 2007. Numerical simulation and experimental investigation of gas–powder flow from radially symmetrical nozzles in laser-based direct metal deposition. International Journal of Machine Tools and Manufacturers 47, 112–123.